


Grain-boundary thermodynamics with artificial-neural-network potential: Its ability to predict the atomic structures, energetics, and lattice vibrational properties for Al

Tatsuya Yokoi ^{1,*}, Maya Matsuura,¹ Yu Oshima,¹ and Katsuyuki Matsunaga^{1,2}

¹*Department of Materials Physics, Nagoya University, Nagoya 464-8603, Japan*

²*Nanostructures Research Laboratory, Japan Fine Ceramics Center, Nagoya 456-8587, Japan*



(Received 17 January 2023; revised 18 April 2023; accepted 1 May 2023; published 17 May 2023)

An artificial neural network (ANN) potential for Al, trained with density-functional-theory (DFT) data, is constructed to accurately predict lattice vibrational properties and thermodynamics of grain boundaries (GBs) in Al. The ANN potential is demonstrated to accurately predict not only atomic structures and energetics of the GBs at 0 K but also partial phonon densities of states and vibrational entropies, even for GBs absent in the training data sets. In addition, their total potential energies and atomic forces by DFT at elevated temperatures up to 800 K can also be well reproduced by molecular dynamics with the ANN potential. In contrast, a modified embedded atom method (MEAM) potential shows larger errors in phonon frequencies and atomic forces for atoms at GBs, as well as in the bulk, than the ANN potential. The MEAM potential is thus likely to be inadequate to quantitatively predict thermodynamic properties of GBs, particularly at high temperature. The present ANN potential is also applied to systematically examine thermodynamic stability of asymmetric tilt GBs. It is predicted that for the $\Sigma 9$ system, the GB free-energy profile as a function of inclination angle exhibits a cusp at elevated temperatures, due to its larger vibrational entropies of asymmetric tilt GBs than those of $\Sigma 9$ symmetric tilt GBs.

DOI: [10.1103/PhysRevMaterials.7.053803](https://doi.org/10.1103/PhysRevMaterials.7.053803)

I. INTRODUCTON

In polycrystalline materials, grain boundaries (GBs) inevitably exist and yield distinct atomic structures, as demonstrated by electron microscopy observation and theoretical calculations [1]. For their impacts on polycrystalline properties, GB free energies are a key factor since they are coupled with GB phenomena (e.g., impurity segregation, point-defect formation, and grain growth) and they govern thermodynamic stability, microstructures, and ultimately material properties. It is thus essential to understand an origin of GB free energies at the atomic level, with the goal of better design of polycrystalline materials at finite temperature. Previous thermal grooving measurements indicated that GB energies decrease with increasing temperature [2–5] and that experimental values are often lower than theoretical values at 0 K [6,7]. On the basis of the standard thermodynamics, the temperature dependence of free energy arises from entropy. For pristine GBs in the absence of point defects and impurities, a dominant factor is in principle vibrational entropy: GBs break the periodicity of the atomic configurations of host crystals and profoundly alter lattice vibration modes, which in turn may influence their vibrational entropies and thereby thermodynamic stability. However, this effect is difficult to quantitatively measure with experiment alone because accumulation of impurities at GBs can substantially affect GB energies [5]. In addition, thermal grooving measurements provide only relative values of GB energies and surface energies and thus cannot identify which one changes with temperature. This leads to the difficulty of extracting vibrational entropies of GBs. To date, little is

known about the relationship between GB free energy and vibrational entropy at the atomic level, particularly in a high-temperature regime.

For this issue, density-functional-theory (DFT) calculations have been employed extensively. Lattice dynamics calculations were performed with the harmonic and quasiharmonic approximations in order to determine phonon modes and thermodynamic quantities for GBs [8,9]. It was indicated that the temperature dependence of vibrational entropies and free energies varies with individual GB structures due to their differences in atomic environment such as bond lengths and coordination numbers [9]. However, GBs typically have lower symmetry in atomic structure than the perfect crystal, particularly for high Σ values and high Miller indices. This substantially increases the required number of atoms in the simulation cells and thereby of single-point calculations for obtaining force constants in lattice dynamics calculations. In addition, modeling of GBs requires larger cell dimensions and more atoms than that of perfect crystals to satisfy the periodic boundary conditions. This is a serious obstacle for DFT studies to examine crystallographically complicated GBs, although such GBs must be addressed to understand general GBs in actual polycrystals. Long-time molecular dynamics (MD) simulations with sufficient statistical accuracy are also essential to examine GB free energies at elevated temperatures, for which the anharmonic effects may become large, but such DFT calculations are not feasible. For these reasons, most DFT studies are limited to simple, high-symmetry systems such as coherent $\Sigma 3$ twins and low- Σ symmetric tilt GBs (STGBs).

Empirical interatomic potentials have also been employed to examine GB thermodynamics [10–15] due to much lower computational cost than DFT calculations. With this

*yokoi@mp.pse.nagoya-u.ac.jp

approach, thermodynamic integration methods were performed to assess anharmonicity in GB free energies [13,15]. A drawback of empirical potentials, however, is the limited transferability to GBs even for atomic structures and energetics at 0 K [16–18]. This is primarily because their empirical parameters are fitted to only bulk properties without consideration of lattice defects. In addition, empirical potentials are typically based on physically inspired analytic functions with simple functional forms, which may lead to a lack of flexibility in approximation of the potential energy surfaces for various atomic environments. To determine thermodynamic properties, one also needs to calculate atomic forces and lattice vibrational modes, which typically requires higher accuracy than determining only atomic structures and energetics at 0 K. This requirement is often difficult to satisfy by means of conventional empirical potentials even without lattice defects [19–22].

To predict lattice vibration behavior and relevant properties with low computational cost and high accuracy, machine-learning (ML) interatomic potentials have become a promising tool [23–27]. This type of potential uses ML models to approximate the potential energy surfaces of DFT calculations through supervised learning with DFT data such as the total potential energies, atomic forces, and stress tensors. After it is trained, it can be combined with molecular simulation algorithms in the same manner as empirical potentials. Current major approaches are based on artificial neural networks [28,29] and Gaussian process regressions [30,31]. Previous studies demonstrated that ML potentials accurately predict the energetics of various lattice defects for metals [32–34], alloys [35,36], and semiconductors [37]. To our knowledge, however, there is still no study that has constructed a single ML potential applicable to various GBs at not only 0 K but also elevated temperature with sufficient accuracy. Additionally, no study has quantitatively examined the transferability of conventional empirical potentials to thermodynamics of GBs.

In this work, an ANN potential was constructed using large amounts of DFT data and was combined with molecular simulations. Here, Al was chosen as it is one of the most fundamental systems and thus the obtained knowledge will be applicable to a wide range of metals and alloys. The predictive ability was then examined with respect to atomic structures, energetics, and vibrational properties for GBs by performing structural relaxation and lattice dynamics. Furthermore, their total energies and atomic forces at finite temperatures were evaluated by performing ANN-driven MD simulations since accurate prediction of these quantities is essential for revealing anharmonicity in GB free energy. Similarly, the transferability of a modified embedded atom method (MEAM) potential [38] to GBs was also elucidated. As a case study of complicated GBs, thermodynamic properties of asymmetric tilt GBs (ATGBs) were ultimately predicted to demonstrate an efficient use of ANN molecular simulations.

II. METHODOLOGY

A. DFT calculation

DFT calculations were performed using projector augmented wave pseudopotentials [39,40] implemented in the

Vienna *Ab initio* simulation package (VASP) [41,42]. Wave functions were described using a plane-wave basis set with a cutoff energy of 450 eV. The exchange-correlation energy was calculated using a revised version of the generalized gradient approximation parametrized by Perdew, Burke, and Ernzerhof (GGA-PBEsol) [43]. The convergence criterion for self-consistent calculation was set to 10^{-6} eV, and $14 \times 14 \times 14$ k -point meshes were used for a cubic unit cell. DFT-MD simulations based on the Parrinello-Rahman dynamics with the Langevin thermostat [44,45] were performed to generate training data sets, as described in the next section. Both *NVT* and *NPT* conditions were used with a time step of 2 fs.

B. Training data set

Table I summarizes the training data sets. The choice of the structures contained was based on our previous study of Si [46], which examined necessary training data sets for ANN potentials to accurately predict the energetics of GB structures. It was found that training data sets consisting of only single crystals led to the limited predictive performance of ANN potentials, with a systematic overestimation of DFT energies, and that GB structures need to be included in training data sets. Following this previous result, not only single crystals but also GB structures were contained in the training data sets. Seven STGBs with the [001] and $[1\bar{1}0]$ rotational axes were modeled by varying the misorientation angle of two grains. In obtaining reference structures for each of the GBs, multiple simulation cells were set up by rigidly shifting one grain relative to the other along the GB plane in an incremental manner. The simulation cells were then relaxed by performing DFT calculations with the conditions mentioned in Sec. II A, and were used as reference structures for generating the training data sets. Surfaces with the (001), (110), (111), and (112) planes were also considered so that the ANN potential is applicable to simulation cells with free surfaces, which were used to predict GB energies and the lowest-energy structures of GBs, as will be shown in Figs. 6 and 7.

The DFT data sets were generated by performing structural relaxation and MD simulation. For a simulation cell in structural relaxation, atoms were randomly displaced by a maximum displacement of 0.2 Å from their initial positions in each direction in the Cartesian coordinate system, and also the cell dimension and shape were randomly changed in the range of $\pm 5\%$. In addition, large expansion and contraction were considered by changing the cell dimensions of four-atom cells in the range of $\pm 20\%$. The simulation cells were then structurally relaxed for 5–20 iterations, and snapshots in this calculation were used as the training data sets. Using reference structures, MD simulations were also performed by varying temperature from 100 to 1000 K, for around 500 steps at each temperature. High temperatures of 1500, 2000, and 2500 K were also considered to generate highly disordered structures. Then snapshots were extracted from the MD results.

C. Construction of ANN potential

The ANN potential was based on the architecture reported by Behler and Parrinello [28] and reviewed by Behler [29], with two hidden layers each having 48 nodes. The activation

TABLE I. Training data sets of single-crystal, surface, and GB structures. N_{str} and N_{force} are the number of total energies and atomic forces for training the ANN potential, respectively. N_{atom} is the number of atoms contained in a simulation cell.

Data set	N_{str}	N_{atom}	N_{force}	MAE		
				Energy (meV/atom)	Force (meV/Å)	
Single crystal	18600	2–32	655287	2.00	13.10	
Surface	21100	8–24	582450	2.06	25.35	
GB	$\Sigma 3(112)/[1\bar{1}0]$	6400	24–48	332850	1.21	18.98
	$\Sigma 5(210)/[001]$	6000	36–40	249050	0.76	16.30
	$\Sigma 5(310)/[001]$	5500	36–40	317700	0.87	19.43
	$\Sigma 9(114)/[1\bar{1}0]$	4800	68–72	508956	0.60	14.70
	$\Sigma 9(221)/[1\bar{1}0]$	5500	32–36	283164	1.14	16.58
	$\Sigma 11(113)/[1\bar{1}0]$	5200	18–22	164442	0.93	13.97
	$\Sigma 19(331)/[1\bar{1}0]$	5500	38–72	457356	0.67	14.38

function was chosen to be the hyperbolic tangent function. To input the information of a crystal structure to the ANN potential, symmetry functions [28,29] were used as atomic descriptors. The two- and three-body descriptors for the i th atom are given by

$$G_i^2 = \sum_{j=1} e^{-\eta_2(R_{ij}-R_s)^2} f_c(R_{ij}), \quad (1)$$

$$G_i^3 = 2^{1-\zeta} \sum_{j \neq i} \sum_{k \neq i,j} \{[1 + \cos(\theta_{ijk} - \theta)]^\zeta e^{-\eta_3(R_{ij}^2 + R_{ik}^2 + R_{jk}^2)} \times f_c(R_{ij})f_c(R_{ik})f_c(R_{jk})\}, \quad (2)$$

respectively. R_{ij} , R_{ik} , and R_{jk} are the distances between atoms ij , ik , and jk , respectively, and θ_{ijk} is the angle between bonds ij and ik . The hyperparameters η_2 , R_s , ζ , θ , and η_3 were empirically determined as listed in Tables S1 and S2 in the supplemental material [47]. These hyperparameters are the same as those in our previous studies of Si and Ge [48]. A cosine cutoff function $f_c(R_{ij})$ was used in the form

$$f_c(R_{ij}) = \begin{cases} \frac{1}{2} [\cos(\frac{\pi R_{ij}}{R_c}) + 1] & (R_{ij} \leq R_c), \\ 0 & (R_{ij} > R_c). \end{cases} \quad (3)$$

The cutoff distance R_c was set to 7 Å. Note that our test calculation evaluated mean absolute errors (MAEs) in training datasets for single crystals by varying R_c from 5 to 8 Å with an increment of 0.5 Å, and $R_c = 7$ Å was found to provide the lowest MAE. To facilitate the training of the ANN potential, the values of the symmetry functions were normalized using the z -score normalization.

The potential fit was performed using an extended Kalman filter with weighted least squares [49] and minibatch learning. The Levenberg-Marquardt method with batch learning was then run for several hundreds of training iterations in order to decrease errors for all training data sets at the same time. Figure 1 shows the correlation between the ANN and DFT values for the training data sets. All data points are distributed close to the diagonal line for both the total energy and the atomic force, indicating that the ANN potential has successfully learned not only single crystals but also GBs. The MAE values are evaluated to be 1.46 meV and 17.1 meV/Å for the total energies per atom and the atomic forces, respectively. These values are comparable to previous studies with ML po-

tentials [17,23], suggesting that the ANN potential maintains a reasonable accuracy to GBs, as demonstrated in Sec. III.

D. Molecular simulation with ANN potential

The trained ANN potential was combined with structural relaxation that adopts a nonlinear conjugate gradient method with the Polak-Ribière formula, in order to predict relaxed structures of GBs. It is noted that one GB often has not only the lowest-energy atomic structure but also local-minimum (often referred to as “metastable”) structures, as for most of the GBs considered. To examine whether the ANN potential can distinguish various energy states and predict the lowest-energy one, multiple simulation cells were constructed in the same manner as that in Sec. II B. Then their relaxed structures and GB energies were initially predicted using the ANN potential. The ANN structures were used to perform DFT single-point calculations and to compare the DFT and ANN results, as will be shown in Fig. 6. This comparison was made for five GBs in the training datasets and for three GBs that were not used for the ANN construction.

The ANN potential was also combined with lattice dynamics and MD simulation in order to examine its predictive ability for vibrational properties and energetics at finite temperature. Lattice dynamics based on the finite displacement method was carried out using the PHONOPY code [50] in the framework of the harmonic approximation. The displacement of an atom was set to 0.01 Å. The relationship between atomic displacements and atomic forces was then calculated using the

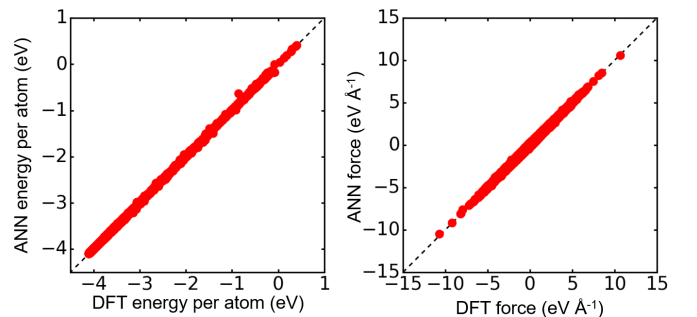


FIG. 1. Correlation between the ANN and DFT values for all training data sets: (a) the total energy and (b) the atomic force.

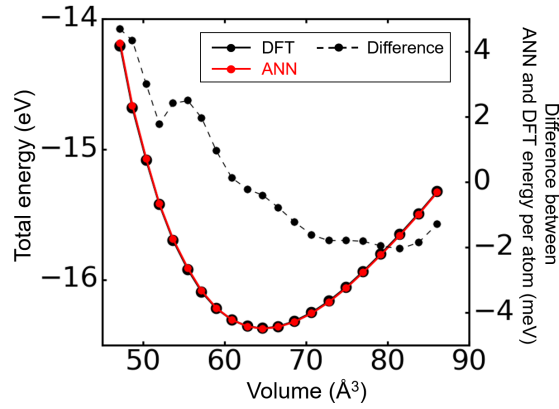


FIG. 2. Energy-volume curves obtained from ANN and DFT calculations for the perfect crystal. The dashed curve corresponds to the difference between the ANN and DFT energies at each volume.

ANN potential in order to obtain second-order force constants and thermodynamic quantities. DFT lattice dynamics was also performed using the same reference cells as those for ANN lattice dynamics.

In the harmonic approximation, the Helmholtz free energy F at temperature T is given by

$$F = E_{\text{static}} + E_{\text{vib}} - TS_{\text{vib}}, \quad (4)$$

where E_{static} is the total potential energy calculated by DFT calculation, and E_{vib} and S_{vib} are the vibrational internal energy and the vibrational entropy, respectively, which were computed by performing lattice dynamics calculations. The GB free energy per unit area of the GB plane γ is calculated by

$$\gamma = \frac{F_{\text{GB}} - F_{\text{Perfect}}}{A}, \quad (5)$$

where F_{GB} and F_{Perfect} are the Helmholtz free energies of supercells of a GB structure and a perfect crystal, respectively, and A is the cross-sectional area of the GB plane. S_{vib} is given by

$$S_{\text{vib}} = \frac{1}{2T} \sum_k \hbar\omega_i \coth\left(\frac{\hbar\omega_i}{2k_B T}\right) - k_B \sum_i \ln\left[2 \sinh\left(\frac{\hbar\omega_i}{2k_B T}\right)\right], \quad (6)$$

where \hbar is the reduced Planck constant, k_B is the Boltzmann constant, and ω_i is the phonon frequency of the j th mode. The atom-projected vibrational entropy of an atom $S_{\text{vib}}^{\text{atom}}$ is calculated by

$$S_{\text{vib}}^{\text{atom}} = \frac{1}{2T} \sum_i \sum_j |e_i(k, j)|^2 \hbar\omega_i \coth\left(\frac{\hbar\omega_i}{2k_B T}\right) - k_B \sum_i \sum_j |e_i(k, j)|^2 \ln\left[2 \sinh\left(\frac{\hbar\omega_i}{2k_B T}\right)\right], \quad (7)$$

where $e_i(k, j)$ is the polarization vector of the i th Cartesian component for wave vector \mathbf{k} and mode j . The sum of $S_{\text{vib}}^{\text{atom}}$ over all atoms in the simulation cell is equal to S_{vib} .

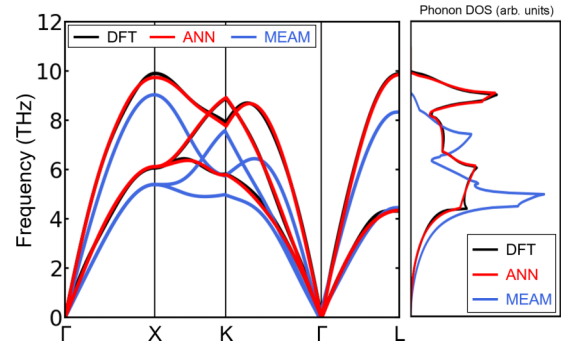


FIG. 3. Phonon dispersion and density of states (DOS) obtained by DFT, ANN, and MEAM calculations for the perfect crystal.

Additionally, ANN-MD simulations were performed at 200, 400, 600, and 800 K. Langevin dynamics with the NVT condition was used, and the total time step was set to 20 ps with a time step of 1 fs at each of the temperatures. Using snapshots extracted with an interval of 1000 steps, the total energies and atomic forces were calculated using the ANN potential and DFT calculations.

The transferability of an MEAM potential [38] to GBs at 0 K and finite temperature was also examined with the GULP package [51] for structural relaxation and MD simulation and with the PHONOPY package [50] for lattice dynamics.

III. RESULTS AND DISCUSSION

A. Bulk properties

This section discusses the predictive ability of the present ANN potential in terms of bulk properties at 0 K and finite temperatures. Figure 2 shows the total potential energies against volume for the face-centered-cubic unit cell. The ANN potential accurately predicts the DFT curve in the entire range of volume, although the error systematically increases by contraction. The equilibrium lattice constant is predicted to be 4.016 Å, which is identical to the DFT value of 4.016 Å. The ANN potential thus shows a sufficient accuracy to predict the potential energy in equilibrium for the perfect crystal.

Figure 3 compares the dispersion curve and density of states (DOS) of phonons for a $6 \times 6 \times 6$ supercell of the primi-

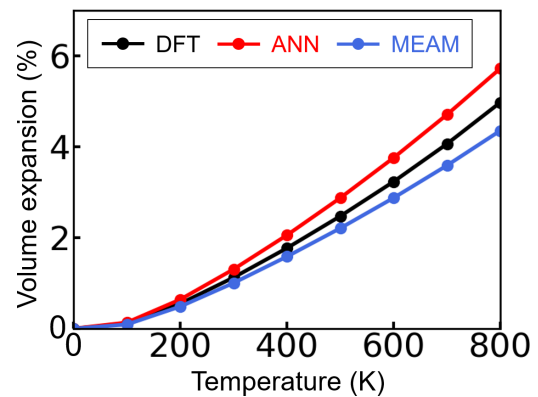


FIG. 4. Volume expansion as a function of temperature for DFT, ANN, and MEAM calculations.

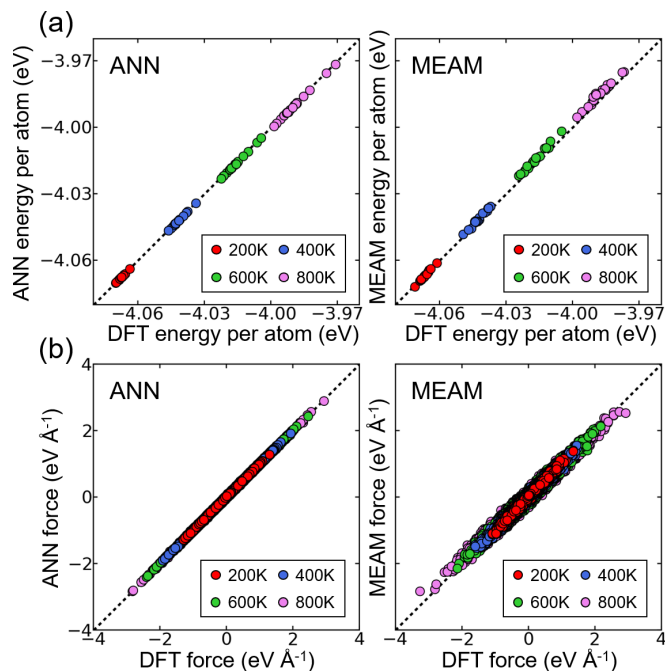


FIG. 5. Correlation between DFT and ANN/MEAM calculations for MD simulations at 200, 400, 600, and 800 K: (a) the total potential energy and (b) the atomic force. Note that the MEAM potential energy of the perfect crystal is shifted to the corresponding DFT value, and the energy difference between the two values is subtracted from all other MEAM energies.

tive cell. The ANN potential reproduces the dispersion curve by DFT for all the phonon bands and hence yields the accurate DOS curve over all the frequencies, capturing the characteristic features, e.g., the prominent peak at 9.1 THz and the minor peak at 6.1 THz. For the MEAM potential, although its low-frequency bands near the Γ point agree with the DFT result, there are clear underestimations at near the X and K points. This leads to erroneous descriptions of the phonon DOS, particularly at frequencies of around 6–8 THz.

The remaining analyses in this section are performed with a $4 \times 4 \times 4$ supercell of the cubic unit cell. Figure 4 shows the temperature dependence of volume expansion based on the quasiharmonic approximation. Although the ANN potential overestimates the DFT value in the entire temperature range, it still maintains a reasonable accuracy with a maximum difference of 0.81% at 800 K. The reason for the overestimation is probably that for expansions of simulation cells in the quasiharmonic approximation, the ANN potential tends to underestimate DFT free energies due to slight underestimations in phonon DOS, as shown in Fig. S1 in the supplemental material [47]. The MEAM potential also exhibits a comparable accuracy to the ANN potential despite the fact that the MEAM phonon modes involve deviations from the DFT modes as indicated by Fig. 3. The reason for the reasonable accuracy is presumably that multiple errors in the phonon modes for the MEAM potential are canceled in calculation of free energies, leading to the small error in volume expansion.

The total energies and atomic forces at finite temperatures are also evaluated by performing MD simulations, as shown in Fig. 5. The MAE value at each of the temperatures is given in

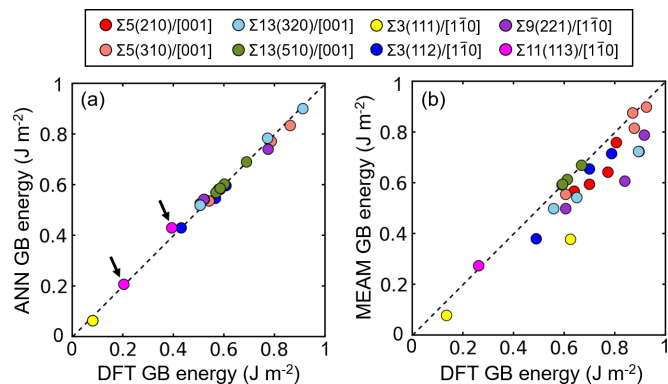


FIG. 6. Correlation of DFT GB energies to (a) ANN and (b) MEAM values. Here, the GB energy is defined as the difference in potential energy per GB area between the GB and the perfect crystal, with the assumption that the two systems have the same number of atoms.

Table II. For the ANN potential, all data points are distributed on the diagonal lines for all cases, without large errors even for high energies and large atomic forces. The maximum MAEs for the total energies and atomic forces are calculated to be 0.80 meV/atom and 12.77 meV/Å at 800 K, respectively. These values are comparable to those for the training data sets and a previous study by Bochkarev *et al.* [23]

The MEAM potential also shows an accuracy comparable to the ANN potential for total energies at 200 K, with an MAE of 0.35 meV/atom, as shown in the top-right panel in Fig. 5(a). However, there is an increasing overestimation with temperature as all data points deviate from the diagonal line. It follows that the MAE increases with increasing temperature, reaching 2.91 meV/atom at 800 K. For the MEAM forces [the bottom-right panel in Fig. 5(b)], although their directions agree with the DFT values, the data points are more scattered than the ANN results, particularly at 800 K. There is also a tendency for the MEAM potential to underestimate DFT forces. The MAE values are between 32.47 and 72.80 meV/Å, which are about five to six times larger than the ANN values.

The above comparisons suggest that for the perfect crystal, the ANN potential predicts vibrational properties at not only low but also high temperatures with much better accuracy than the MEAM. The MEAM potential also shows a reasonable accuracy, but it involves the erroneous description of phonon modes and also shows the increased errors in total energy and atomic force at elevated temperatures. It thus may be difficult for the MEAM potential to quantitatively predict free energies at high temperatures even for the perfect crystal.

B. Atomic structures and energetics of GBs at 0 K

The accurate determination of low-energy structures and energetics of the GBs at 0 K, which is addressed in this section, is a prerequisite since they are used as reference structures for assessing vibrational and thermodynamic properties. Figure 6 shows the correlation of DFT GB energies to ANN and MEAM values. As mentioned in Sec. IID, a GB often has not only the lowest-energy but also metastable structures, and thus their values are also plotted.

TABLE II. MAE values of total energies and atomic forces in MD simulations for the bulk.

Temperature (K)	MAE			
	Total energy (meV/atom)		Atomic force (meV/Å)	
	ANN	MEAM	ANN	MEAM
200	0.35	0.35	5.99	32.47
400	0.54	1.02	8.58	46.30
600	0.68	2.31	10.72	58.91
800	0.80	2.91	12.77	72.80

For the ANN potential [Fig. 6(a)], all data points are located close to the diagonal line from low to high GB energies, with an MAE of 13.4 mJ/m². Importantly, the lowest-energy structures predicted by the ANN potential are also the lowest-energy ones in the DFT level for all GBs examined; as an example of $\Sigma 11(113)$, the order of the two GB energies pointed by the arrows is the same between the ANN and DFT results. It also accurately reproduces the relative GB energies of different atomic structures for one GB. This enables us to identify possible metastable structures, which is essential for understanding GB-structure transformation at a finite temperature as indicated in the literature [15,52]. It is noteworthy that the ANN potential maintains a sufficient accuracy to predict the GB energies for $\Sigma 13(510)$ and $\Sigma 13(320)$ despite their absence in the training data sets. It is thus expected that the present ANN potential is generalizable to crystallographically various GBs, enabling us to gain insight into general GBs, as addressed later in Sec. III E.

For the MEAM potential [Fig. 6(b)], although there is a positive correlation between the MEAM and DFT values, the data points are more scattered than the ANN results, with underestimation of DFT values. The MAE for all GB structures is found to be 109.1 mJ/m², which is about eight times larger than the ANN value. Thus, a quantitative comparison between the relative stability of GB structures appears to be difficult on the basis of MEAM prediction, which also may lead to the difficulty of quantitatively reproducing the transformation between GB structures. It is noted for the MEAM potential that a GB tends to have more metastable structures than that for the ANN potential, e.g., as observed for the $\Sigma 3(111)$ GB (yellow points). The metastable structure for the MEAM potential was relaxed by performing DFT calculations. As a result, it transformed to the lowest-energy structure. This thus may indicate that the MEAM potential energy surface at GBs has metastable structures that are not local minima in the DFT level.

Figure 7 shows the lowest-energy structures predicted by the ANN potential for the GBs examined. Their structural units agree with previous theoretical studies [53–55]. In addition, their atomic arrangements were almost unchanged after DFT structural relaxation, which is also the case for $\Sigma 13(510)$ and $\Sigma 13(320)$. Thus, the ANN potential enables us to quantitatively predict both lowest-energy structures and their GB energies even for GBs not included in the training data sets.

The MEAM potential also predicts the ANN structures in Fig. 7 to be in the lowest-energy states, except for $\Sigma 3(112)$. It is thus likely that the MEAM potential also can be used to search for the lowest-energy structures for many GBs in

AI. Nevertheless, careful validation should be made: DFT calculations indicate that for $\Sigma 3(112)$, the MEAM structure (the rightmost panel in Fig. 7) is higher in GB energy by 0.02 J/m² than the ANN structure. This implies that the MEAM potential involves an erroneous description of the potential energy surface for $\Sigma 3(112)$, thereby failing to find its exact structure. Although it is unclear whether such error also occurs in more complicated GBs, a similar situation presumably occurs at least for $\Sigma 3(112)$ -containing GBs, such as $\Sigma 3$ ATGBs with the $[1\bar{1}0]$ axis.

C. Lattice vibrational properties of GBs

In this section, the transferability of the ANN and MEAM potentials to lattice vibrational properties of the GBs is evaluated within the harmonic approximation. Figure 8 shows errors of atom-projected vibrational entropies ($S_{\text{vib}}^{\text{atom}}$) at 700 K for the GB atoms. Here, atoms at a GB are regarded as “GB atoms” if they have either coordination numbers different from 12 or average bond lengths different by more than 1.4% from that in the bulk. This threshold for the bond length was empirically determined to extract all atoms constituting the structural units for all GBs examined. The ANN prediction [Fig. 8(a)] indicates that all data points, including those of $\Sigma 13(320)$ and $\Sigma 13(510)$, are distributed close to the diagonal line, with an MAE of 0.26 J K⁻¹ mol⁻¹. The maximum error is also reasonably small with 1.31 J K⁻¹ mol⁻¹ for the $\Sigma 5(310)$ atom, as labeled A.

Figure 8(b) indicates that the MEAM potential also predicts $S_{\text{vib}}^{\text{atom}}$ with a reasonable accuracy as data points are located near the diagonal line, with an MAE of 0.82 J K⁻¹ mol⁻¹ for all data points. However, there are underestimated and overestimated values, depending on each GB atom, and certain GB atoms exhibit noticeable deviations from the DFT values. For example, data points A and B involve errors of 2.32 and 4.68 J K⁻¹ mol⁻¹, respectively. Such deviation may become critical with increasing $S_{\text{vib}}^{\text{atom}}$ in prediction of thermodynamic properties of GBs unless those errors are effectively canceled, since large $S_{\text{vib}}^{\text{atom}}$ more significantly affects the temperature dependence of the free energy.

The deviations in $S_{\text{vib}}^{\text{atom}}$ for the MEAM potential arise from erroneous descriptions in partial phonon DOS. Two examples are shown in Fig. 9. Atoms A and B in Fig. 8(a) are located in the structural units in the insets in Fig. 9. For atom A [Fig. 9(a)], the DFT and ANN curves indicate the largest peak at 2.1 THz and the second largest peak at 4.7 THz, while the MEAM potential predicts the largest peak to appear at 5.3 THz. For atom B [Fig. 9(b)], the DFT and ANN results

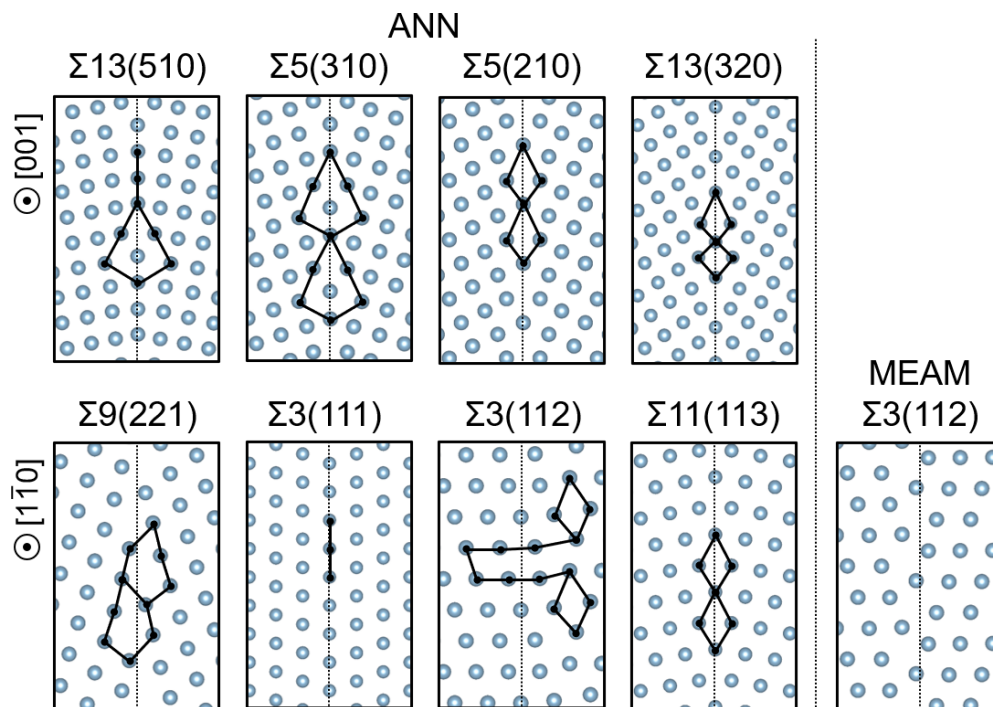


FIG. 7. Lowest-energy structures predicted by the ANN potential for symmetric tilt GBs with the [001] and [1 $\bar{1}$ 0] rotational axes. The black lines and polyhedra represent structural units that are conventionally defined in the literature [53–55]. The rightmost panel shows the lowest-energy $\Sigma 3(112)$ structure predicted from the MEAM potential.

indicate that the largest peak is at 0.9 THz and three minor peaks are present in the range between 2.6 and 6.1 THz. For the MEAM potential, the largest peak slightly deviates up from the DFT curve by 0.4 THz, and also the positions of the minor peaks are not consistent with those of the corresponding DFT peaks. These errors are not canceled and consequently

yield the large deviations in S_{vib}^{atom} from the DFT value [see Fig. 8(b)]. The other GB atoms also involve more or less errors in partial phonon DOS, as shown in Fig. S2 in the supplemental material [47].

Figure 10 plots the temperature dependence of γ based on the harmonic approximation. The γ value at 0 K is set to be zero. The slopes of the profiles arise from the vibrational entropies of atoms as shown in Fig. 8. The ANN potential more accurately predicts the temperature dependence of the GB free energies by DFT calculations than the MEAM potential, except for $\Sigma 9(221)$. In addition, the errors of the ANN potential are less than about 0.03 J/m² at 800 K, demonstrating that it predicts GB free energies with high accuracy. It is noted here that the profiles for $\Sigma 5(310)$ and $\Sigma 13(510)$ by the MEAM potential are close to the ones by DFT despite the errors in partial phonon DOS and thereby in S_{vib}^{atom} , as indicated

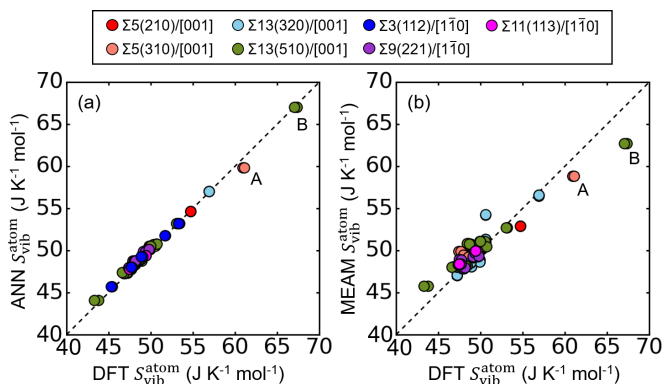


FIG. 8. Errors in atom-projected vibrational entropies (S_{vib}^{atom}) of GB atoms at 700 K for (a) the ANN potential and (b) the MEAM potential. The lowest-energy structures in Fig. 7 were fully relaxed by performing DFT or interatomic-potential calculations, and then lattice dynamics calculations with the harmonic approximation were performed using each of the methods. Note that $\Sigma 3(111)$ does not have GB atoms and thus its data point is absent. It is also noted that the MEAM result does not contain $\Sigma 3(112)$ values because the MEAM lowest-energy structure is different from the lowest-energy one for DFT calculations. The data points labeled A and B correspond to the atoms whose partial phonon DOS is depicted in Fig. 9.

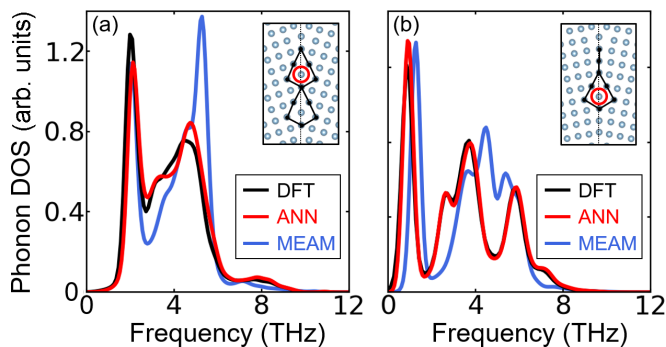


FIG. 9. Partial phonon DOS for the GB atoms encircled in red for (a) $\Sigma 5(310)$ and (b) $\Sigma 13(510)$, which correspond to atoms A and B in Fig. 8, respectively.

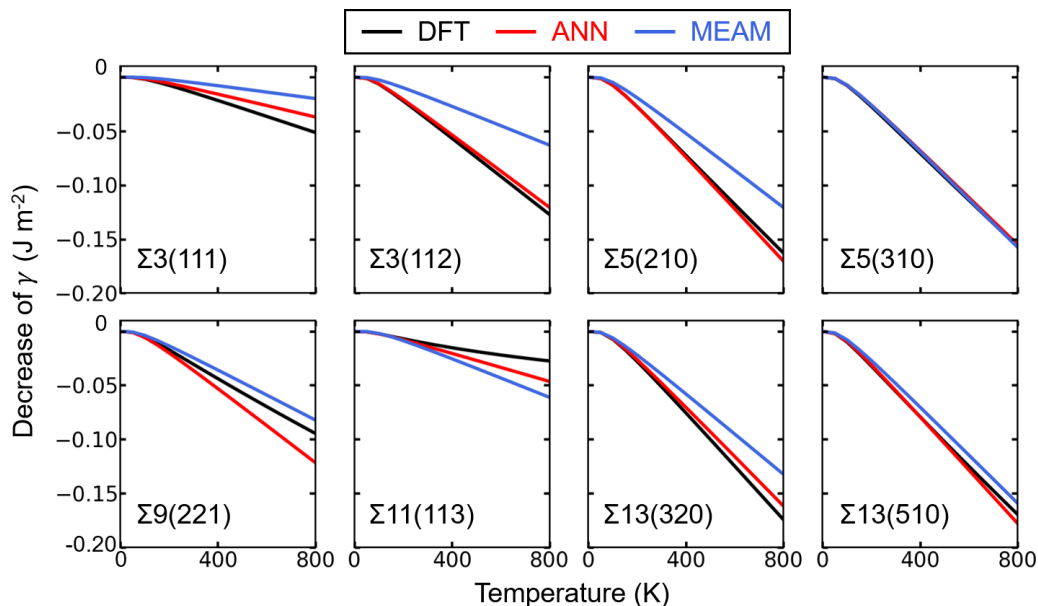


FIG. 10. Decrease in GB free energy (γ) from the values at 0 K for each of the GBs examined.

by Figs. 8 and 9. It is speculated that underestimated and overestimated $S_{\text{vib}}^{\text{atom}}$ values at the GB atoms are canceled by summing those values, resulting in the MEAM results close to the DFT values.

D. Finite-temperature energetics of GBs

The results in the previous section are based on the harmonic approximation. This section discusses the energetics of the GBs in MD simulations, for which anharmonicity may become more pronounced with rising temperature. Figure 11 shows MAE values of total potential energies evaluated from snapshots in MD simulations at 200, 400, 600, and 800 K. Figure 11(a) indicates that the ANN potential reason-

ably predicts total potential energies for all GBs, although the MAE values for $\Sigma 5(310)$ and $\Sigma 9(221)$ are larger than those for the other GBs. Table III lists the average MAEs over all GBs at the respective temperatures. These values are similar to each other regardless of temperature, ranging between 0.9×10^2 and 1.1×10^2 J/m², demonstrating the transferability of the ANN potential to the entire temperature range. Figure 11(b) indicates that the MAE values of the MEAM potential depend strongly on the GBs and temperature, with large values for some cases. For example, the MAE for $\Sigma 13(510)$ ranges between 1.0×10^2 and 1.4×10^2 J/m², whereas that for $\Sigma 11(113)$ is in the range of 6.4×10^2 and 10.4×10^2 J/m²; for $\Sigma 3(111)$, the MAE values are evaluated to be 0.8×10^2 J/m² at 200 K and 7.1×10^2 J/m² at 800 K.

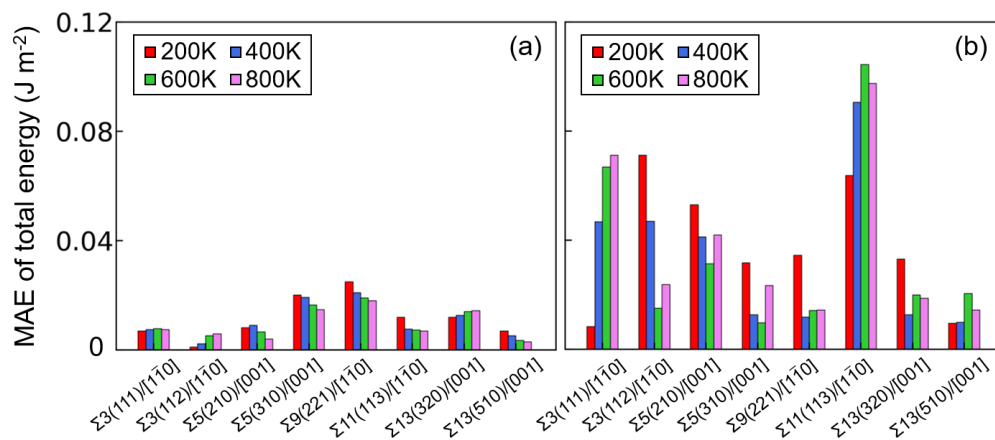


FIG. 11. MAE values of the total potential energies in MD simulations for (a) the ANN potential and (b) the MEAM potential with respect to those by DFT calculations. These values are evaluated by averaging the errors of 20 snapshots during MD simulations. Note that the MAE of total energy per atom for a system just provides an averaged values for bulk and GB atoms, and that errors due to bulk atoms are typically very small. Thus, MAE values are seemingly small if one uses a GB simulation cell with a wide bulk region. To eliminate this effect and quantitatively evaluate errors due to GB atoms, GB energies obtained by DFT and the ANN/MEAM potentials were compared. In this case, the unit of an MAE value is given by J/m².

TABLE III. MAE values of total energies and atomic forces in MD simulations for all GBs examined.

Temperature (K)	MAE			
	Total energy (J/m ²)		Atomic force (meV/Å)	
	ANN	MEAM	ANN	MEAM
200	0.011	0.038	12.92	69.82
400	0.010	0.034	16.17	84.11
600	0.010	0.035	19.04	96.48
800	0.009	0.038	21.56	110.00

Figure 12 shows that the errors of the individual snapshots used in Fig. 11 are evaluated at each of the temperatures for $\Sigma 3(112)$ and $\Sigma 11(113)$. The results of the other GBs are indicated by Fig. S3 in the supplemental material [47]. For the ANN potential, the data points show no deviation from the diagonal line at all temperatures. On the other hand, the MEAM potential tends to underestimate the total energies of $\Sigma 3(112)$ at lower temperatures of 200 and 400 K, whereas it systematically overestimates the DFT values for $\Sigma 11(113)$ at all temperatures. This suggests that the MEAM potential is unable to accurately predict the total potential energies depending on the temperature range or the GB types.

Figure 13 shows errors in atomic forces during MD simulations at the different temperatures. Figure 13(a) indicates that the ANN potential has MAE values ranging from 7.6 to 23.3 meV/Å, depending on the temperatures. These values are around twice the bulk values listed in Table II, but they are still comparable to those reported in a previous ML-potential study that examined formation free energies for a monovacancy in Al [23]. The MAE values for the different GBs are also in the same level and are independent of the GB structures, suggesting the predictive power of the present ANN potential for the GBs.

For the MEAM potential [Fig. 13(b)], the MAE values are larger than those of the ANN potential for all the GBs, ranging from 28.2 to 128.3 meV/Å. For many of the GBs, the MAE values exceed 100 meV/Å at 600 and 800 K, suggesting a less predictive ability in terms of atomic forces for the GB atoms (see also Table III). As an example of $\Sigma 5(210)$, Fig. 14 shows the correlations atomic forces obtained by DFT. The MEAM potential shows more scattered data points than the ANN potential, with a tendency to underestimate DFT values for large atomic forces at elevated temperatures. A similar trend is observed for all GBs examined (Fig. S4 in the supplemental material [47]) and for the perfect crystal (Fig. 5). This may indicate that for GBs at high temperature, the slope of the potential energy surface for the MEAM potential is entirely smaller than the DFT result, and hence MEAM vibrational modes have lower frequencies than DFT ones. Considering the above results, the ANN potential is expected to be more suitable to quantitatively examine GB thermodynamics at the wider temperature range, as compared to the conventional MEAM potential.

As provided in the supplemental material [47], an additional analysis was conducted for more complex GBs than [001]- and $[1\bar{1}0]$ -axis STGBs. For this purpose, three GBs were chosen: the $\Sigma 5(001)$ twist GB with a twist angle of 36.87° , the $\Sigma 39(\bar{7}25)/[111]$ STGB, and the $\Sigma 5(430)|| (100)/[001]$ ATGB. The test data sets were generated by performing ANN-MD simulations in the same manner as that mentioned above. The ANN potential is found to exhibit a more excellent predictive performance than the MEAM potential for all cases, with MAE values similar to those shown in Figs. 11 and 13. This supports the idea that the transferability of our ANN potential is not limited to specific data sets of STGBs with the [001] and $[1\bar{1}0]$ axes.

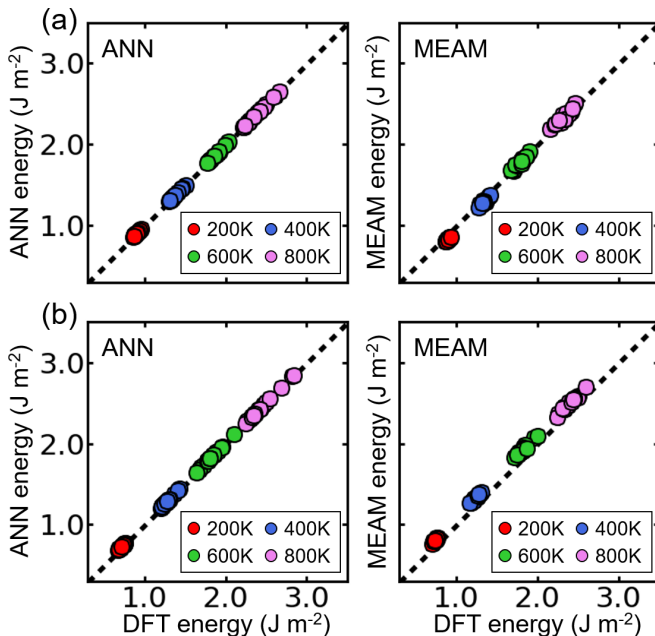


FIG. 12. Errors in total potential energies during MD simulations for (a) $\Sigma 3(112)$ and (b) $\Sigma 11(113)$.

E. Application of ANN potential to complicated GBs

As a case study of complicated GBs for which DFT analysis is computationally demanding, the ANN potential was applied to ATGBs. For an ATGB, two grains have differently oriented planes at the interface while a STGB consists of two grains in contact with crystallographically the same plane. In actual polycrystals, ATGBs are most likely to be more dominant than STGBs except for particular cases (e.g., $\Sigma 3$ twin GBs). Thus, systematic analysis of free energies for ATGBs is of importance for understanding thermodynamics of polycrystals. To our knowledge, however, there are no theoretical studies that have systematically examined ATGBs at finite temperatures.

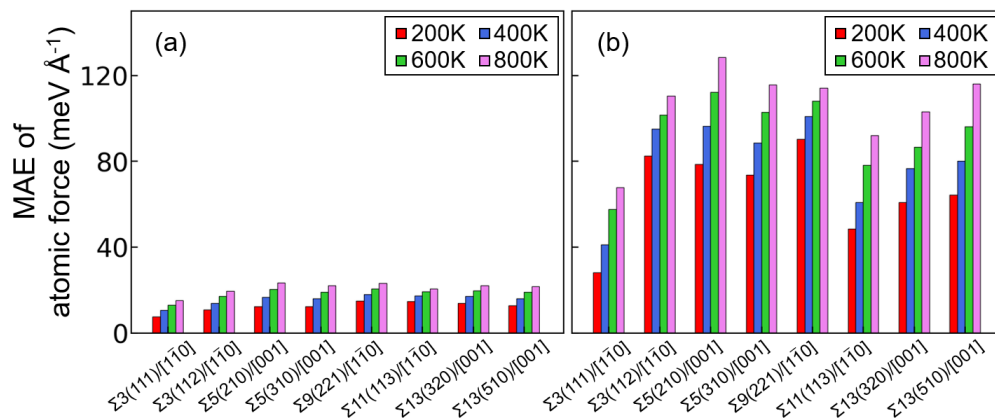


FIG. 13. MAE values of atomic forces acting on GB atoms in MD simulations for (a) the ANN potential and (b) the MEAM potential. Note that $\Sigma 3(111)$ has no GB atoms, and thus the atoms on the interfacial plane are regarded as GB atoms. The atomic forces are obtained from the same snapshots used for calculating the MAE values in total energies (Fig. 11).

Here, ATGBs with the $[001]$ and $[1\bar{1}0]$ rotational axes were examined by considering the systems of $\Sigma = 3, 5, 9, 11,$ and 13 . Their lowest-energy structures were determined by performing structural relaxation in the same manner as mentioned in Secs. II B and II D. The obtained structures agree with calculated structures for Cu [54,55]. The structural data are provided in the supplemental material [47].

Figure 15 shows their thermodynamic quantities calculated using the harmonic approximation with the ANN potential. The crystallography of an ATGB is characterized by not only the misorientation angle of two grains, as for STGBs, but also the GB plane. The inclination angle Φ is thus introduced to define the rotation angle of a GB plane about the tilt axis. STGBs correspond to $\Phi = 0^\circ, 45^\circ$ and $\Phi = 0^\circ, 90^\circ$ for the $[001]$ and $[1\bar{1}0]$ systems, respectively. For ATGBs belonging to a Σ system, the misorientation angle is the same regardless of Φ , whereas the GB planes differ with Φ . The GB energy at 0 K (γ^0) and the GB vibrational entropy (S_{GB}) at T were also defined in the same manner as γ in Eq. (5).

For ATGBs with $\Sigma = 3, 5,$ and 13 , the computed and theoretical values of γ^0 are close to each other, indicating that these ATGBs ideally dissociate into STGBs with faceted interfaces. For the $\Sigma 9$ and $\Sigma 11$ systems, on the other hand, the computed γ^0 are lower than their theoretical values. This is because $\Sigma 9$ and $\Sigma 11$ ATGBs favor dissociation into structural

units different from those for STGBs with the same Σ system. These trends are similar to those in previous studies of ATGBs in Cu and Al [54,55].

For the $\Sigma 5$ and $\Sigma 13$ ATGBs, the computed S_{GB} and γ follow their theoretical values, as might be expected. However, the $\Sigma 3$ ATGBs indicate the computed S_{GB} to be slightly larger than the theoretical values, although all $\Sigma 3$ ATGBs examined dissociate into the $\Sigma 3(111)$ and $\Sigma 3(112)$ structural units. The $\Sigma 11$ ATGBs also exhibit a similar trend in S_{GB} to the $\Sigma 3$ ATGBs. Interestingly, the S_{GB} values of the $\Sigma 9$ ATGBs examined are entirely larger than those of the $\Sigma 9(221)$ and $\Sigma 9(114)$ STGBs, which causes the γ curve to have a clear cusp at 700 K for the $\Sigma 9(111)/(115)$ ATGB ($\Phi = 35.3^\circ$). This suggests that $\Sigma 9$ ATGBs are energetically higher than the $\Sigma 9(221)$ and $\Sigma 9(114)$ GBs at 0 K but become more stable at elevated temperature, due to the larger S_{GB} . It thus may be anticipated that favorable distributions of GBs show some temperature dependence for certain Σ systems. For this issue, further research will be needed by considering general GBs and taking into account anharmonic effects.

To specify atoms having the largest impact on S_{GB} for $\Sigma 9(111)/(115)$, the S_{GB} value is decomposed into $S_{\text{vib}}^{\text{atom}}$ for each atom, as depicted in Fig. 16(a). It is found that the atom located at the junction of two structural units has the highest value of $S_{\text{vib}}^{\text{atom}}$, as indicated by the black arrow. This GB atom is 13-fold coordinated with an average bond length of 3.01 Å. Such an atom, which is typically absent in the lowest-energy structures of low- Σ STGBs, may be key to determining thermodynamics of ATGBs with faceted interfaces. Figure 16(b) compares the partial phonon DOS for the GB atom with the largest $S_{\text{vib}}^{\text{atom}}$ and the bulk atom. The GB atom is found to have a prominent peak at 1.7 THz, which is absent for the bulk atom, and it shows phonons shifting toward low-frequency modes. According to the harmonic approximation, if phonons shift entirely toward lower-frequency modes, the vibrational entropy generally increases [50]. Thus the strong low-frequency peak for the GB atom results in a substantial increase in $S_{\text{vib}}^{\text{atom}}$ and thereby in S_{GB} for $\Sigma 9(111)/(115)$.

It is noted that the above analyses use only the lowest-energy structures at 0 K as references to examine GB free energies. Previous theoretical studies indicated that for a GB,

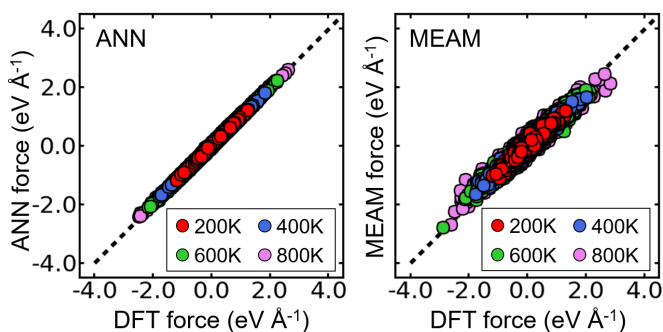


FIG. 14. Errors in atomic forces of GB atoms during MD simulation for $\Sigma 5(210)$.

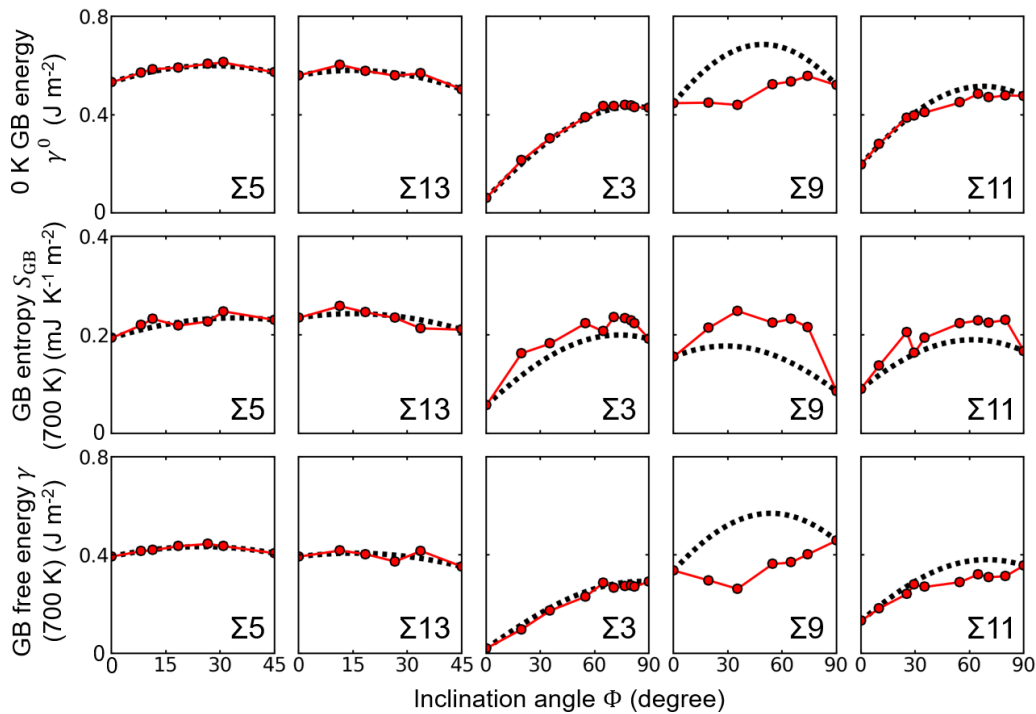


FIG. 15. ANN prediction of GB energy at 0 K (γ^0), GB vibrational entropy (S_{GB}) at 700 K, and GB free energy (γ) at 700 K (the bottom panels). The dashed lines represent the theoretical values when asymmetric tilt GBs ideally facet to the symmetric tilt GBs without energy penalty [54,55].

certain metastable structures at 0 K become more stable than the lowest-energy structure at 0 K with increasing temperature [9,11]. This may also occur for ATGBs because most of the ATGBs examined are found to have multiple metastable structures at 0 K. This issue should be addressed in future work by applying ANN-driven lattice dynamics to not only the lowest-energy structures but also metastable structures and comparing their thermodynamic stability at each temperature.

IV. CONCLUSIONS

An ANN potential was trained using large amounts of DFT data and was combined with structural relaxation, MD

simulation, and lattice dynamics calculation, with the goal of achieving high-accuracy prediction with respect to thermodynamic quantities for GBs in Al. The ANN potential was found to accurately predict not only atomic structures and energetics at 0 K but also partial phonon DOS and atom-projected vibrational entropies for GB atoms, even for GBs absent in the training data sets. The predictive power is also maintained for total potential energies and atomic forces at not only low but also high temperatures, at which anharmonic effects may become non-negligible. The ANN potential is thus expected to enable us to systematically understand vibrational properties and thermodynamics of general GBs in a wide range of temperature.

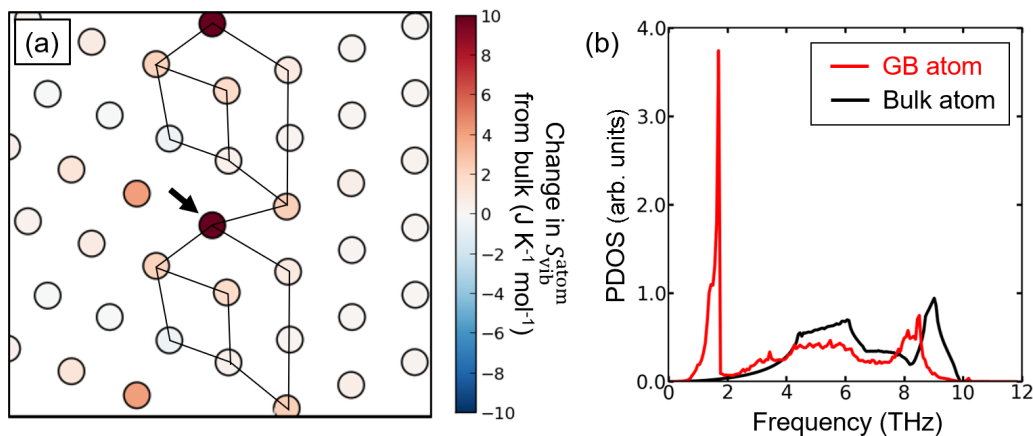


FIG. 16. (a) Changes in S_{vib}^{atom} from the bulk value for each atoms in the $\Sigma 9(111)/(115)$ ATGB. The atomic positions are viewed along the $[1\bar{1}0]$ direction. The black lines represent structural units. (b) The partial phonon DOS of the GB atom indicated by the black arrow in Fig. 16(a). For comparison, the phonon DOS of the bulk atom is also plotted.

For the MEAM potential, the lowest-energy structures were consistent with the ANN and DFT ones except for $\Sigma 3(112)$. However, the predicted relative stability of GB structures involved errors and entirely underestimated DFT values. For some GB atoms, the MEAM potential involved erroneous reproductions of their partial phonon DOS, leading to larger errors in $S_{\text{vib}}^{\text{atom}}$ than the ANN values. It was also found that errors in MEAM free energy significantly varied with individual GBs and temperatures. This will be an obstacle to quantitatively examine more complicated GBs for which DFT validation is not feasible. For MD simulations, MEAM atomic forces for GB atoms exhibited entirely larger errors than the ANN values, with MAE values exceeding 100 meV/Å at 600 and 800 K. Thus, although the MEAM potential can be used to qualitatively predict low-energy atomic structures, it may be difficult to use to quantitatively predict thermodynamic quantities of GBs, particularly at high temperature.

The ANN potential was ultimately used to predict GB free energies for ATGBs, as a case study of complicated GBs.

$\Sigma 9$ ATGBs exhibited larger vibrational entropies than the $\Sigma 9(221)$ and $\Sigma 9(114)$ STGBs, and as a result, they became thermodynamically more stable than the $\Sigma 9$ STGBs at elevated temperatures. This may affect favorable distributions of GBs in polycrystals at finite temperature.

ACKNOWLEDGMENTS

The work was supported by JSPS KAKENHI (JP19H05786, JP21K14405, and JP22H04508), JST-CREST (JPMJCR17J1), and “Joint Usage/Research Center for Interdisciplinary Large-scale Information Infrastructures” in Japan (Project ID: jh220057). This work was also supported by Toyota-Riken-scholar program and CHUBEI ITOH FOUNDATION. DFT calculations and molecular simulations with the ANN potential were partly performed with the facilities of the Supercomputer Center, the Institute for Solid State Physics, the University of Tokyo.

-
- [1] K. Matsunaga, M. Yoshiya, N. Shibata, H. Ohta, and T. Mizoguchi, Ceramic science of crystal defect cores, *J. Ceram. Soc. Jpn.* **130**, 648 (2022).
- [2] D. W. Readey and R. E. Jech, Energies and grooving kinetics of [001] tilt boundaries in nickel oxide, *J. Am. Ceram. Soc.* **51**, 201 (1968).
- [3] H. Miura, M. Kato, and T. Mori, Temperature dependence of the energy of Cu [110] symmetric tilt grain boundaries, *J. Mater. Sci. Lett.* **13**, 46 (1994).
- [4] A. Tsoga and P. Nikolopoulos, Surface and grain-boundary energies in yttria-stabilized zirconia (YSZ-8 mol%), *J. Mater. Sci.* **31**, 5409 (1996).
- [5] M. N. Kelly, S. A. Bojarski, and G. S. Rohrer, The temperature dependence of the relative grain-boundary energy of yttria-doped alumina, *J. Am. Ceram. Soc.* **100**, 783 (2017).
- [6] U. Wolf, F. Ernst, T. Muschik, M. W. Finnis, and H. F. Fischmeister, The influence of grain boundary inclination on the structure and energy of $\sigma = 3$ grain boundaries in copper, *Philos. Mag. A* **66**, 991 (1992).
- [7] H. Nishimura, K. Matsunaga, T. Saito, T. Yamamoto, and Y. Ikuhara, Atomic structures and energies of $\Sigma 7$ symmetrical tilt grain boundaries in alumina bicrystals, *J. Am. Ceram. Soc.* **86**, 574 (2003).
- [8] D. Scheiber, O. Renk, M. Popov, and L. Romaner, Temperature dependence of surface and grain boundary energies from first principles, *Phys. Rev. B* **101**, 174103 (2020).
- [9] T. Yokoi, K. Ikawa, A. Nakamura, and K. Matsunaga, An origin of excess vibrational entropies at grain boundaries in Al, Si and MgO: A first-principles analysis with lattice dynamics, *Phys. Chem. Chem. Phys.* **23**, 10118 (2021).
- [10] M. Hashimoto, Y. Ishida, R. Yamamoto, and M. Doyama, Thermodynamic properties of coincidence boundaries in aluminum, *Acta Metall.* **29**, 617 (1981).
- [11] R. Najafabadi, D. J. Srolovitz, and R. LeSar, Thermodynamic and structural properties of [001] twist boundaries in gold, *J. Mater. Res.* **6**, 999 (1991).
- [12] A. Hairie, F. Hairie, B. Lebouvier, G. Nouet, E. Paumier, N. Ralantson, and A. P. Sutton, Free energies of interfaces from quasi-harmonic theory: A critical appraisal, *Interface Sci.* **2**, 17 (1994).
- [13] S. M. Foiles, Evaluation of harmonic methods for calculating the free energy of defects in solids, *Phys. Rev. B* **49**, 14930 (1994).
- [14] S. M. Foiles, Temperature dependence of grain boundary free energy and elastic constants, *Scr. Mater.* **62**, 231 (2010).
- [15] R. Freitas, R. E. Rudd, M. Asta, and T. Frolov, Free energy of grain boundary phases: Atomistic calculations for $\Sigma 5(310)$ [001] grain boundary in Cu, *Phys. Rev. Mater.* **2**, 093603 (2018).
- [16] D. Scheiber, R. Pippan, P. Puschnig, and L. Romaner, Ab initio calculations of grain boundaries in bcc metals, *Modell. Simul. Mater. Sci. Eng.* **24**, 035013 (2016).
- [17] T. Nishiyama, A. Seko, and I. Tanaka, Application of machine learning potentials to predict grain boundary properties in fcc element metals, *Phys. Rev. Mater.* **4**, 123607 (2020).
- [18] Y. Shihara, R. Kanazawa, D. Matsunaka, I. Lobzenko, T. Tsuru, M. Kohyama, and H. Mori, Artificial neural network molecular mechanics of iron grain boundaries, *Scr. Mater.* **207**, 114268 (2022).
- [19] M. Khalkhali, Q. Liu, and H. Zhang, A comparison of different empirical potentials in ZnS, *Modell. Simul. Mater. Sci. Eng.* **22**, 085014 (2014).
- [20] P. Rowe, G. Csányi, D. Alfè, and A. Michaelides, Development of a machine learning potential for graphene, *Phys. Rev. B* **97**, 054303 (2018).
- [21] H. Babaei, R. Guo, A. Hashemi, and S. Lee, Machine-learning-based interatomic potential for phonon transport in perfect crystalline Si and crystalline Si with vacancies, *Phys. Rev. Mater.* **3**, 074603 (2019).
- [22] E. Torres, I. Cheik Njifon, T. P. Kakoni, and J. Pencer, A comparative analysis of the phonon properties in UO₂ using the Boltzmann transport equation coupled with DFT+U and empirical potentials, *Comput. Mater. Sci.* **177**, 109594 (2020).
- [23] A. S. Bochkarev, A. van Roekeghem, S. Mossa, and N. Mingo, Anharmonic thermodynamics of vacancies using a neural network potential, *Phys. Rev. Mater.* **3**, 093803 (2019).

- [24] G. Mangold, S. Chen, G. Barbalinardo, J. Behler, P. Pochet, K. Termentzidis, Y. Han, L. Chaput, D. Lacroix, and D. Donadio, Transferability of neural network potentials for varying stoichiometry: Phonons and thermal conductivity of Mn_xGe_y compounds, *J. Appl. Phys.* **127**, 244901 (2020).
- [25] Y.-B. Liu, J.-Y. Yang, G.-M. Xin, L.-H. Liu, G. Csányi, and B.-Y. Cao, Machine learning interatomic potential developed for molecular simulations on thermal properties of $\beta\text{-Ga}_2\text{O}_3$, *J. Chem. Phys.* **153**, 144501 (2020).
- [26] J. M. Choi, K. Lee, S. Kim, M. Moon, W. Jeong, and S. Han, Accelerated computation of lattice thermal conductivity using neural network interatomic potentials, *Comput. Mater. Sci.* **211**, 111472 (2022).
- [27] Z. Wei C. Zhang, Y. Kan, Y. Zhang, and Y. Chen, Developing machine learning potential for classical molecular dynamics simulation with superior phonon properties, *Comput. Mater. Sci.* **202**, 111012 (2022).
- [28] J. Behler and M. Parrinello, Generalized Neural-Network Representation of High-Dimensional Potential-Energy Surface, *Phys. Rev. Lett.* **98**, 146401 (2007).
- [29] J. Behler, Constructing high-dimensional neural network potentials: A tutorial review, *Int. J. Quantum Chem.* **115**, 1032 (2015).
- [30] A. P. Bartók, M. C. Payne, R. Kondor, and G. Csányi, Gaussian Approximation Potentials: The Accuracy of Quantum Mechanics, without the Electrons, *Phys. Rev. Lett.* **104**, 136403 (2010).
- [31] A. P. Bartók and G. Csányi, Gaussian Approximation Potentials: A Brief Tutorial Introduction, *Int. J. Quantum Chem.* **115**, 1051 (2015).
- [32] D. Dragoni, T. D. Daff, G. Csányi, and N. Marzari, Achieving DFT accuracy with a machine-learning interatomic potential: Thermomechanics and defects in bcc ferromagnetic iron, *Phys. Rev. Mater.* **2**, 013808 (2018).
- [33] M. Stricker, B. Yin, E. Mak, and W. A. Curtin, Machine learning for metallurgy II. A neural-network potential for magnesium, *Phys. Rev. Mater.* **4**, 103602 (2020).
- [34] J. Byggmästar, A. Hamedani, K. Nordlund, and F. Djurabekova, Machine-learning interatomic potential for radiation damage and defects in tungsten, *Phys. Rev. B* **100**, 144105 (2019).
- [35] D. Marchand, A. Jain, A. Glensk, and W. A. Curtin, Machine learning for metallurgy I. A neural-network potential for Al-Cu, *Phys. Rev. Mater.* **4**, 103601 (2020).
- [36] A. C. P. Jain, D. Marchand, A. Glensk, M. Ceriotti, and W. A. Curtin, Machine learning for metallurgy III. A neural-network potential for Al-Mg-Si, *Phys. Rev. Mater.* **5**, 053805 (2021).
- [37] A. P. Bartók, J. Kermode, N. Bernstein, and G. Csányi, Machine Learning a General-Purpose Interatomic Potential for Silicon, *Phys. Rev. X* **8**, 041048 (2018).
- [38] B.-J. Lee, J.-H. Shim, and M. I. Baskes, Semiempirical atomic potentials for the fcc metals Cu, Ag, Au, Ni, Pd, Al, and Pb based on first and second nearest-neighbor modified embedded atom method, *Phys. Rev. B* **68**, 144112 (2003).
- [39] P. E. Elöchl, Projector augmented-wave method, *Phys. Rev. B* **50**, 17953 (1994).
- [40] G. Kresse and D. Joubert, From ultrasoft pseudopotentials to the projector augmented-wave method, *Phys. Rev. B* **59**, 1758 (1999).
- [41] G. Kresse and J. Furthmüller, Efficiency of ab-initio total energy calculations for metals and semiconductors using a plane-wave basis set, *Comput. Mater. Sci.* **6**, 15 (1996).
- [42] G. Kresse and J. Furthmüller, Efficient iterative schemes for ab initio total-energy calculations using a plane-wave basis set, *Phys. Rev. B* **54**, 11169 (1996).
- [43] J. P. Perdew, A. Ruzsinszky, G. I. Csonka, O. A. Vydrov, G. E. Scuseria, L. A. Constantin, X. Zhou, and K. Burke, Restoring the Density-Gradient Expansion for Exchange in Solids and Surfaces, *Phys. Rev. Lett.* **100**, 136406 (2008).
- [44] M. Parrinello and A. Rahman, Crystal Structure and Pair Potentials: A Molecular-Dynamics Study, *Phys. Rev. Lett.* **45**, 1196 (1980).
- [45] M. Parrinello and A. Rahman, Polymorphic transitions in single crystals: A new molecular dynamics method, *J. Appl. Phys.* **52**, 7182 (1981).
- [46] T. Yokoi, Y. Noda, A. Nakamura, and K. Matsunaga, Neural-network interatomic potential for grain boundary structures and their energetics in silicon, *Phys. Rev. Mater.* **4**, 014605 (2020).
- [47] See Supplemental Material at <http://link.aps.org/supplemental/10.1103/PhysRevMaterials.7.053803> for the hyperparameters of symmetry functions, free energies calculated from the quasiharmonic approximation and phonon DOS for expanded simulation cells, the partial phonon DOS of GB atoms for all the GBs examined, errors in total energy and atomic force during MD simulations, and the calculated atomic structures of ATGBs.
- [48] T. Yokoi, H. Kato, Y. Oshima, and K. Matsunaga, Atomic structures of grain boundaries for Si and Ge: A simulated annealing method with artificial-neural-network interatomic potentials, *J. Phys. Chem. Solids* **173**, 111114 (2023).
- [49] T. B. Blank and S. D. Brown, Adaptive, global, extended Kalman filters for training feedforward neural networks, *J. Chemom.* **8**, 391 (1994).
- [50] A. Togo and I. Tanaka, First principles phonon calculations in materials science, *Scr. Mater.* **108**, 1 (2015).
- [51] J. D. Gale, GULP: A computer program for the symmetry-adapted simulation of solids, *J. Chem. Soc., Faraday Trans.* **93**, 629 (1997).
- [52] T. Meiners, T. Frolov, R. E. Rudd, G. Dehm, and C. H. Liebscher, Observations of grain-boundary phase transformations in an elemental metal, *Nature (London)* **579**, 375 (2020).
- [53] M. Rajagopalan, M. A. Bhatia, M. A. Tschopp, D. J. Srolovitz, and K. N. Solanki, Atomic-scale analysis of liquid-gallium embrittlement of aluminum grain boundaries, *Acta Mater.* **73**, 312 (2014).
- [54] M. A. Tschopp and D. L. McDowell, Structures and energies of $\Sigma 3$ asymmetric tilt grain boundaries in copper and aluminium, *Philos. Mag.* **87**, 3147 (2007).
- [55] M. A. Tschopp and D. L. McDowell, Asymmetric tilt grain boundary structure and energy in copper and aluminium, *Philos. Mag.* **87**, 3871 (2007).